Low Temperature Physics/Fizika Nizkikh Temperatur, 2012, v. 38, No. 7, pp. 703–714

Magnetooptic coupling coefficients for one- and two-magnon Raman scattering in the rutile-structure antiferromagnets FeF_2, MnF_2, CoF_2 and NiF_2

D.J. Lockwood

Institute for Microstructural Sciences, National Research Council, Ottawa, Ontario, Canada K1A 0R6
E-mail: David.Lockwood@nrc-cnrc.gc.ca

M.G. Cottam

Department of Physics and Astronomy, University of Western Ontario, London, Ontario, Canada N6A 3K7
E-mail: cottam@uwo.ca

Received March 28, 2012

Inelastic light scattering intensities of magnetic excitations are governed by the magnetooptic coupling coefficients, which have been evaluated, for example, for the ferrimagnet $Y_3Fe_5O_{12}$ (YIG) and the metamagnets $FeCl_2$ and $FeBr_2$. However, by far the most detailed studies to date have been performed on the classic rutile-structure antiferromagnets, and we summarize here the results obtained from the many experimental and theoretical investigations in these compounds for both one-magnon and two-magnon excitations. A comparison of the magnitudes of the various coupling coefficients for MnF_2, FeF_2, CoF_2, and NiF_2 reveals a surprising similarity in many coefficients. In one-magnon Raman scattering, the in-phase linear magnetooptic coefficient dominates and the main differences between MnF_2, FeF_2, and NiF_2 lie in the relative significance of the in-phase quadratic magnetooptic coefficient. Thus the quadratic coefficients are now seen to be of particular importance in determining the strength of the one-magnon scattering in a variety of magnetic insulators. In two-magnon Raman scattering, one magnetooptic coefficient dominates for all of these antiferromagnets. However, each of the other six coefficients are remarkably similar in magnitude, in general, and not negligible in most cases, indicating some universality in the way light interacts with the pairs of magnons of opposite and equal wave vector in rutile structure antiferromagnets.

PACS: 75.50.Ee Antiferromagnetics;
78.30.–j Infrared and Raman spectra;
75.30.Ds Spin waves.

Keywords: magnetooptic, antiferromagnet, spin wave or magnon, Raman scattering.

In Celebration of Professor V.V. Eremenko's 80th Birthday

1. Introduction

For many years now inelastic light (Raman) scattering [1] has been usefully employed to characterize low lying excitations in magnetic systems [2]. The Raman spectrum provides information on the frequency, line width, and intensity of the excitation, which is usually studied in Stokes scattering only, and measurements of its polarization dependence provide details on the symmetry of the scattering. Investigations of the temperature and applied magnetic field dependence of the scattering from such excitations, which include magnons and excitons, have now become routine [2]. The results of these studies have been extensively analyzed theoretically with regard to the excitation frequency, line shape, and line width, as well as their temperature and field dependences. One piece of information that so far has seldom been investigated is the intensity of the excitation, using information from both Stokes and anti-Stokes Raman scattering measurements. Light scattering intensities of magnetic excitations are governed by the so-called magnetooptic coupling coefficients [2–4], which have so far been explored for the ferrimagnet $Y_3Fe_5O_{12}$ (YIG) [5], in this case by Brillouin scattering, and the metamagnets $FeCl_2$ and $FeBr_2$ [6–8]. However, the most detailed studies to date have been performed on the classic rutile-structure antiferromagnets [2], and it is

Table 1. Physical parameters of rutile-structure antiferromagnets. This information is taken from Ref. 2

Compound	Neél temperature T_N, K	Spin S	Spin alignment	Other factors
FeF_2	78	2	Along c axis	Optic modes
MnF_2	68	5/2	Along c axis	Pure spin
CoF_2	38	Effective spin of 3/2	Along c axis	Spin-orbit coupling
				Optic modes
				Single-ion anisotropy
NiF_2	73	1	In ab plane and canted	Single-ion anisotropy

the results from these Raman scattering investigations for both one-magnon and two-magnon excitations that are reviewed below.

Light scattering from magnons in rutile-structure (space group $P4_2/mnm$ or D_{4h}^{14}) antiferromagnets has been extensively studied because of their fairly simple magnetic ordering [2]. The examples we consider here are FeF_2, MnF_2, CoF_2 and NiF_2 and their physical properties relevant to antiferromagnetism are summarized in Table 1. The antiferromagnetically ordered crystal structure of the first three compounds is shown schematically in Fig. 1. Below the ordering temperature, T_N, the transition-metal-ion spins align along the crystal c axis in opposing fashion (see Fig. 1) to produce the overall antiferromagnetic arrangement of spins. The magnetic properties of these three compounds differ because of the following factors: MnF_2 has a very small anisotropy and is essentially a pure spin antiferromagnet; FeF_2 exhibits optic magnons and possesses a large anisotropy; and CoF_2 has strong spin-orbit coupling along with a number of higher lying electronic states within the ground multiplet. FeF_2 and MnF_2, in particular, have been extensively studied because of the relative simplicity of their magnetic interactions and the theoretical results for the acoustic and optic magnons are in good agreement with experimental data over a broad range of temperatures [2]. On the other hand, the one-magnon light scattering in CoF_2 has other distinctive properties due to effects arising from a strong orbital angular momentum and a large single-ion anisotropy. Although the two-magnon scattering can be analyzed within a simple effective spin $S = 1/2$ model [9], the one-magnon scattering case is much more complicated and has only recently been fully examined theoretically [10]. By contrast, NiF_2 presents a case of special interest [11] because of the role of the single-ion anisotropy in NiF_2, which causes the sublattice magnetization to lie perpendicular (rather than parallel, as in the above-mentioned cases) to the crystal c axis and to be canted slightly in the ab plane away from the antiparallel alignment. This more unusual spin ordering is shown schematically in Fig. 2. As a consequence, the twofold degeneracy in the one-magnon dispersion is removed since the resulting small net ferromagnetic moment gives rise to an additional low-frequency magnon excitation, which depends sensitively on the canting angle, in addition to the usual higher frequency excitation observed in the other three antiferromagnets, where there is no spin canting.

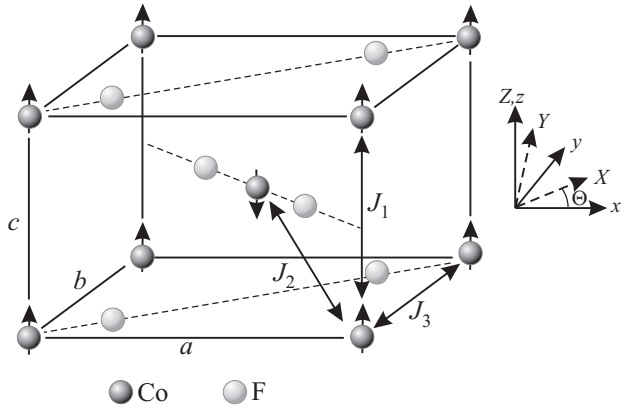

Fig. 1. The crystallographic unit cell of CoF_2 ($a = b \neq c$) showing the c axis spin alignment along with the principal exchange interactions J_1, J_2, and J_3. Crystal axes (x, y, z) and laboratory axes (X, Y, Z) are illustrated in relation to the unit cell. The X and Y directions are orthogonal to the c (Z) axis but are rotated by ~ 45° from the crystallographic a and b axes.

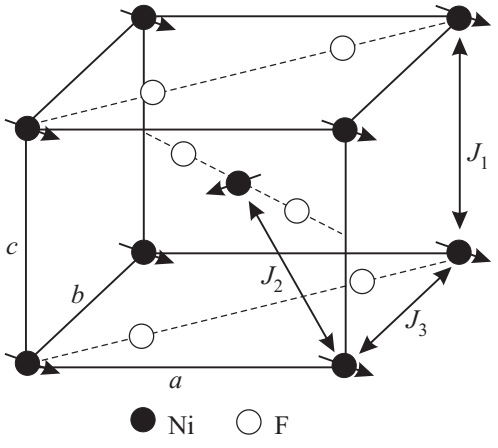

Fig. 2. The crystallographic unit cell of NiF_2 showing the canted spin alignment in the crystal ab plane along with the dominant exchange interactions J_1, J_2, and J_3.

2. Theory

2.1. Spin Hamiltonians and magnon frequencies

The rutile-structure antiferromagnets MnF_2 (spin S = = 5/2) and FeF_2 (S = 2) can be well represented in the case of zero applied magnetic field by the following Heisenberg Hamiltonian with anisotropy terms:

$$H = \sum_{i,j} J_{i,j}\mathbf{S}_i \cdot \mathbf{S}_j + \frac{1}{2}\sum_{i,i'} J'_{i,i'}\mathbf{S}_i \cdot \mathbf{S}_{i'} +$$

$$+ \frac{1}{2}\sum_{j,j'} J'_{j,j'}\mathbf{S}_j \cdot \mathbf{S}_{j'} - g\mu_B H_A(T)(\sum_i S_i^z - \sum_j S_j^z). \quad (1)$$

This includes the effects of the dominant intersublattice exchange J_{ij} and the weaker intrasublattice exchange $J'_{ii'}$ and $J'_{jj'}$, where labels i and j denote spin sites on sublattice 1 (spins predominantly "up") and sublattice 2 (spins "down"), respectively. The interactions between different neighbors are seen in Fig. 1 where the rutile crystal structure is depicted. The quantity $H_A(T)$ represents a temperature-dependent effective anisotropy field for the uniaxial anisotropy.

CoF_2 and NiF_2 exhibit a more complicated magnetic behavior. The exchange part of the Hamiltonian has the same form as above, but the anisotropy has to be represented explicitly with uniaxial D and nonuniaxial F coefficients in the form

$$+\sum_i \left\{D(S_i^z)^2 - F[(S_i^x)^2 - (S_i^y)^2]\right\} +$$

$$+ \sum_j \left\{D(S_j^z)^2 + F[(S_j^x)^2 - (S_j^y)^2]\right\}. \quad (2)$$

In CoF_2 we have $D < 0$ leading to spin alignment along the crystal c axis as in Fig. 1, but an *effective* spin description is needed because of large spin-orbit effects. The simplest model is to take S = 1/2, which is satisfactory for applications to two-magnon Raman scattering, since this is strongly weighted by large wavevectors near the Brillouin zone boundary. However, it leads to discrepancies with Raman experiments for one-magnon scattering, which is weighted by the zone-center wavevectors, and a S = 3/2 model is required instead [10]. In NiF_2 (S = 1) we have $D > |F| > 0$, which results in the equilibrium spin orientations being in the *ab* plane with a small canting from antiparallel alignment, as shown in Fig. 2.

In terms of Eq. (1) for MnF_2 and FeF_2 the simplest theory for the linearized magnon frequency that incorporates the temperature dependence employs the random-phase approximation to decouple the exchange terms. The expression for the frequency $\omega(\mathbf{k})$ at wavevector $\mathbf{k}$ is [2]

$$\omega(\mathbf{k}) = \left\{\mu^2(\mathbf{k}) - [8\langle S^z\rangle J_2 \cos(\frac{1}{2}k_x a)\cos(\frac{1}{2}k_y a)\cos(\frac{1}{2}k_z c)]^2\right\}^{1/2}, \quad (3)$$

where $\langle S^z\rangle$ denotes a thermal average and

$$\mu(\mathbf{k}) = g\mu_B H_A + 2\langle S^z\rangle \times$$

$$\times\left\{4J_2 - J_3\sin^2(\frac{1}{2}k_x a) - J_3\sin^2(\frac{1}{2}k_y a) - J_1\sin^2(\frac{1}{2}k_z c)\right\}. \quad (4)$$

At $\mathbf{k}$ = 0, as in one-magnon Raman scattering, the above result simplifies to

$$\omega(0) = \left\{\omega_A(2\omega_E + \omega_A)\right\}^{1/2}, \quad (5)$$

where $\omega_A = g\mu_B H_A$ and $\omega_E = 8\langle S^z\rangle J_2$ are the anisotropy and exchange frequencies, respectively. Often it is assumed [12] that $\omega_A \propto \langle S^z\rangle^n$ where index n lies between 1 and 2. The above frequency, which is just the antiferromagnetic resonance (AFMR) frequency, can be split into two components by an applied magnetic field.

Equations (3)–(5) are not applicable to CoF_2 and NiF_2, except in the context of two-magnon scattering where the effects of the single-ion anisotropy at large $|\mathbf{k}|$ become small compared with the exchange terms (and then with $\langle S^z\rangle$ replaced by a thermal average in the *ab* plane in the case of NiF_2) [9]. By contrast, at $\mathbf{k}$ = 0 as in one-magnon scattering, it is important to employ Eq. (2) for the single-ion anisotropy (with its uniaxial and nonuniaxial parts). Care must be taken in the Green's function formalism for the magnons to avoid any decoupling of the products of spin operators that occur at the *same* site. The formalism, which is an extension of that due to Awang and Cottam [13], leads to additional magnon branches for both CoF_2 (see Ref. 10) and NiF_2 (Ref. 11) in accordance with experiment.

2.2. Magnetooptical coupling and Raman intensities

Here we follow an approach similar to that employed by Cottam [4] (see also Ref. 2) for two-sublattice antiferromagnets. The interaction Hamiltonian for the inelastic scattering of light depends on the electric-field vectors of the incident and scattered light and on the spin-dependent susceptibility tensor $\chi(\mathbf{r})$ where $\mathbf{r}$ denotes any sublattice spin site. Next the elements of this tensor may be expanded in powers of the spin operators, going up to and including quadratic terms, as

$$\chi^{\alpha\beta}(\mathbf{r}) = \sum_\mu K_{\alpha\beta\mu}(\mathbf{r})S_{\mathbf{r}}^\mu +$$

$$+\sum_{\mu,\nu} G_{\alpha\beta\mu\nu}(\mathbf{r})S_{\mathbf{r}}^\mu S_{\mathbf{r}}^\nu + \sum_{\mu,\nu,\boldsymbol{\delta}} B_{\alpha\beta\mu\nu}(\mathbf{r},\boldsymbol{\delta})S_{\mathbf{r}}^\mu S_{\mathbf{r}+\boldsymbol{\delta}}^\nu \quad (6)$$

Here α, β, μ, and ν denote Cartesian components. The first two terms above involve operators at a single site **r**, while the third term involves products of operators at different sites (connected by vector **δ**). The quantities *K*, *G*, and *B* are related to different magnetooptical effects. In a ferromagnetic material, for example, *K* is proportional to the magnetic circular birefringence (Faraday rotation) and *G* is proportional to the magnetic linear birefringence (Voigt or Cotton–Mouton effect) [5]. In second order of perturbation the light-scattering intensity is related to dynamic correlation functions between one component of χ and another component of χ at a different position and time [2]. Therefore, in view of Eq. (6), it is necessary to evaluate spin–spin correlation functions (or the corresponding Green's functions) to obtain the intensities [4]. The different roles of the terms in Eq. (6) as regards one- and two-magnon light scattering are now outlined below.

2.2.1. One-magnon scattering. Magnons are related to the excitations of a transverse spin component, i.e., S^+ or S^- (where $S^{\pm} = S^x \pm iS^y$). Terms that are linear in $S^{\pm}$ occur not only in the first term (involving the *K* coefficients), but also in the quadratic terms through products like $S^{\pm}S^z$ and $S^zS^{\pm}$. There are two quadratic terms in Eq. (6), but the one that is the more important for the one-magnon scattering is the same-site term that involves the *G* coefficients [4]. The other quadratic spin term (with the *B* coefficients) is mainly of interest for two-magnon scattering and will be discussed later.

The **k** = 0 one-magnon excitations in MnF_2 and FeF_2 are doubly degenerate in zero applied magnetic field with the components having symmetries Γ_3^+ and Γ_4^+ in a standard notation [3]. From a group-theoretical analysis [3], the corresponding Raman scattering matrices have the general form

$$\chi(\Gamma_3^+) = \begin{pmatrix} 0 & 0 & \gamma_1 \\ 0 & 0 & i\gamma_1^* \\ \gamma_2 & i\gamma_2^* & 0 \end{pmatrix}, \quad \chi(\Gamma_4^+) = \begin{pmatrix} 0 & 0 & -\gamma_1 \\ 0 & 0 & i\gamma_1^* \\ -\gamma_2 & i\gamma_2^* & 0 \end{pmatrix}. \tag{7}$$

The complex quantities γ_1 and γ_2 can be related to the one-magnon terms in Eq. (6), giving the expressions [3]

$$\gamma_{1,2} = -\varphi(T) \times$$

$$\times \left[\left(\pm K_+ + 2p\langle S^z \rangle \frac{\omega(0)}{\omega_A} G_+ \right) + i \left(\pm \frac{\omega(0)}{\omega_A} K_- + 2p\langle S^z \rangle G_- \right) \right]. \tag{8}$$

Here $\varphi(T)$ is an overall temperature-dependent factor, while K_+ and G_+ refer to the linear and quadratic magnetooptical coupling terms, respectively, when the two sublattices of spins scatter in phase. They are related to specific combinations of the related coefficients in Eq. (6), as deduced by symmetry. There may also be contributions with K_- and G_- that describe the linear and quadratic coupling for out-of-phase scattering. The latter effects are allowed by symmetry because the two sublattices are not strictly equivalent (due to the coordination of the nonmagnetic F^- ions as in Fig. 1). It can be seen that the relative weightings of the four magneto-optical coefficients in Eq. (8) depend on the ratio of $\omega(0)$ to ω_A and on other temperature-dependent factors, including the parameter *p* which arises in the Green's function theory [4] and can be approximated by $(2S-1)\langle S^z \rangle / 2S^2$.

The integrated intensity I_S for one-magnon Stokes scattering can be deduced from the above results and takes the form [4,14]

$$I_S \propto \frac{\langle S^z \rangle (n_0 + 1)}{\omega(0)} (F_{\text{in}} + F_{\text{out}}), \tag{9}$$

where n_0 is the Bose-Einstein thermal factor for the **k** = 0 magnons with frequency $\omega(0)$, and the in-phase and out-of-phase scattering terms are

$$F_{\text{in}} = \left| e_A^- \omega_A^{1/2} K_+ - 2p\langle S^z \rangle e_S^- (2\omega_E + \omega_A)^{1/2} G_+ \right|^2, \tag{10}$$

$$F_{\text{out}} = \left| e_A^+ (2\omega_E + \omega_A)^{1/2} K_- - 2p\langle S^z \rangle e_S^+ \omega_A^{1/2} G_- \right|^2. \tag{11}$$

The electric-field polarization dependence comes through the symmetric (S) and antisymmetric (A) combinations defined by

$$e_S^{\pm} = (e_1^z e_2^x + e_1^x e_2^z) \pm i(e_1^z e_2^y + e_1^y e_2^z), \tag{12}$$

$$e_A^{\pm} = (e_1^z e_2^x - e_1^x e_2^z) \pm i(e_1^z e_2^y - e_1^y e_2^z), \tag{13}$$

where $\mathbf{e}_1$ and $\mathbf{e}_2$ are the unit polarization vectors for the incident and scattered light, respectively. We note that the linear and quadratic coupling terms are associated with Eqs. (13) and (12), respectively, so a polarization analysis of the experimental data can be used to distinguish between their contributions.

Analogous results for the anti-Stokes scattering intensity [4,14,15] can be written down in a similar fashion. An important conclusion is that the anti-Stokes to Stokes ratio of intensities, which is simply equal to $n_0/(n_0 + 1)$ or $\exp[-\omega(0)/k_BT]$ in many cases, is modified when both linear and quadratic magnetooptical terms contribute.

Finally, the above formalism has to be modified in the cases of CoF_2 and NiF_2. It is still the case for these materials that the linear and quadratic magnetooptical coupling effects may apply, but their effects are different due to the different behavior already mentioned for the **k** = 0 one-magnon excitations [10,11].

2.2.2. Two-magnon scattering. The interaction Hamiltonian for the two magnon scattering of light from a rutile-structure antiferromagnet can be deduced from the last

term in Eq. (6), specifically from the combinations that involve products like S^+S^- and S^zS^z for spins at neighboring sites. It may be written as [2,9,14]

$$H_{\rm int} = \frac{1}{2}\sum_{\mathbf{r},\boldsymbol{\delta}} \phi(\boldsymbol{\delta})(S^+_{\mathbf{r}} S^-_{\mathbf{r}+\boldsymbol{\delta}} + S^-_{\mathbf{r}} S^+_{\mathbf{r}+\boldsymbol{\delta}} + \gamma S^z_{\mathbf{r}} S^z_{\mathbf{r}+\boldsymbol{\delta}}), \quad (14)$$

where $\mathbf{r}$ is summed over all spin sites, vector $\boldsymbol{\delta}$ now connects sites with their next-nearest neighbors (on the opposite sublattice), and γ is a weighting factor. The symmetry term $\phi(\delta)$, which contains the electric-field polarizations, is

$$\phi(\delta) = B_1(e_1^x e_2^x + e_1^y e_2^y) + B_2 e_1^z e_2^z + B_3(e_1^x e_2^y + e_1^y e_2^x)\sigma_\delta^x\sigma_\delta^y +$$

$$+ B_4\left[(e_1^x e_2^z + e_1^z e_2^x)\sigma_\delta^x\sigma_\delta^z + (e_1^y e_2^z + e_1^z e_2^y)\sigma_\delta^y\sigma_\delta^z\right] +$$

$$+ B_5\left[(e_1^x e_2^z - e_1^z e_2^x)\sigma_\delta^x\sigma_\delta^z + (e_1^y e_2^z - e_1^z e_2^y)\sigma_\delta^y\sigma_\delta^z\right] \quad (15)$$

where $\sigma_\delta^\alpha = \mathrm{sign}(\delta^\alpha)$ for $\alpha = x, y, z$, and B_1, B_2, …, B_5 are the two-magnon magnetooptical coupling coefficients. By varying the polarizations in an experiment, one may effectively pick out various combinations of the B coefficients. Another symmetry-allowed contribution to $H_{\rm int}$, which is often neglected, is of the form [9,14]

$$\frac{1}{2}\sum_{\mathbf{r},\delta} \phi'(\delta)(S^+_{\mathbf{r}} S^-_{\mathbf{r}+\delta} - S^-_{\mathbf{r}} S^+_{\mathbf{r}+\delta}), \quad (16)$$

where

$$\phi'(\delta) = iB_6(e_1^x e_2^x - e_1^y e_2^y) + iB_7(e_1^x e_2^y - e_1^y e_2^x)\sigma_\delta^x\sigma_\delta^y. \quad (17)$$

This introduces two additional coefficients B_6 and B_7.

Expressions for the two-magnon Raman scattering intensities are given in Ref. 16, where a finite-temperature Green's function analysis with magnon–magnon interactions was used. For the rutile-structure antiferromagnets there are three Raman-active modes, conventionally labeled [3] as Γ_1^+, Γ_4^+, and Γ_5^+. These have different weighting factors, and so different critical points in the Brillouin zone are emphasized (specifically, the Γ, M, and R points, respectively). Consequently, there is a small splitting in the two-magnon peak frequencies, e.g., estimated to be of order $8\langle S^z\rangle(J_3 - J_1)$ between the Γ_4^+ and Γ_5^+ modes [14,16].

Finally, although we emphasized earlier that CoF_2 and NiF_2 are both very different from the simpler compounds MnF_2 and FeF_2 in their one-magnon Raman spectra, it is nevertheless the case that they can all be treated within the same formalism described above as regards their two-magnon Raman scattering. This is because the two-magnon scattering emphasizes the large wavevector regions (except in the case of the nonresonant Γ_1^+ mode), where the non-uniaxial single-ion anisotropy effects are small.

3. Comparison with experiment

The two-magnon Raman peak parameters of frequency and line width as well as the line shape are analyzed systematically following the theory outlined in the previous section and given in detail in Ref. 2. Such an analysis yields improved values for the three exchange parameters and the anisotropy over those obtained from other techniques (principally inelastic neutron scattering) as the two-magnon peak position and line shape are very sensitive to these values. The parameter values thus obtained for the four antiferromagnets and used in our calculations are summarized in Table 2.

Table 2. Principal exchange interactions J_1, J_2, and J_3 and anisotropy parameters deduced from theoretical analysis of the two-magnon Raman spectrum of rutile-structure antiferromagnets at temperature $T << T_N$. In the cases of CoF_2 and MnF_2 the quoted H_A are effective anisotropy terms as approximated for zone-boundary magnons

Compound	J_1, cm^{-1}	J_2, cm^{-1}	J_3, cm^{-1}	H_A, cm^{-1}
FeF_2 (Ref. 16)	0.01	3.73	0.21	20.0
MnF_2 (Ref. 14)	−0.50	2.48	~0	0.74
CoF_2 (Ref. 9)	−1.2	12.9	~0	12.0
NiF_2 (Ref. 9)	0.2	13.8	0.3	2.1

The theoretical model for one-magnon scattering outlined above involves four magnetooptical coefficients that are independent of temperature and light scattering geometry. These coefficients are denoted by K_+ and G_+ for the linear and quadratic magnetooptical coupling for in-phase scattering, while K_- and G_- are the corresponding coefficients for out-of-phase scattering. For two-magnon scattering there are as many as seven coefficients (B_n with n = = 1, …, 7). We now outline the results obtained for these parameters in four quite different antiferromagnets possessing the rutile crystal structure.

3.1. MnF_2

3.1.1. One-magnon scattering. A typical anti-Stokes–Stokes Raman spectrum is shown in Fig. 3 [17]. This spectrum clearly shows that some factor other than the usual thermal population factor is operating and causing the anti-Stokes Raman peak to be much stronger than the Stokes peak. The important information to be obtained from such spectra for the analysis that follows is the integrated intensities of the Stokes and anti-Stokes one-magnon peaks together with their polarization and temperature dependences.

In making a comparison of theory with experiment for the one-magnon Raman integrated intensities in MnF_2 we have assumed for simplicity that in-phase scattering is dominant. This would be expected because the deviation from tetragonal symmetry at a Mn^{2+} site is relatively small. For the Stokes data in Fig. 4, the theory predicts that $I_S(XZ) = I_S(YZ)$ at any given temperature, whatever the

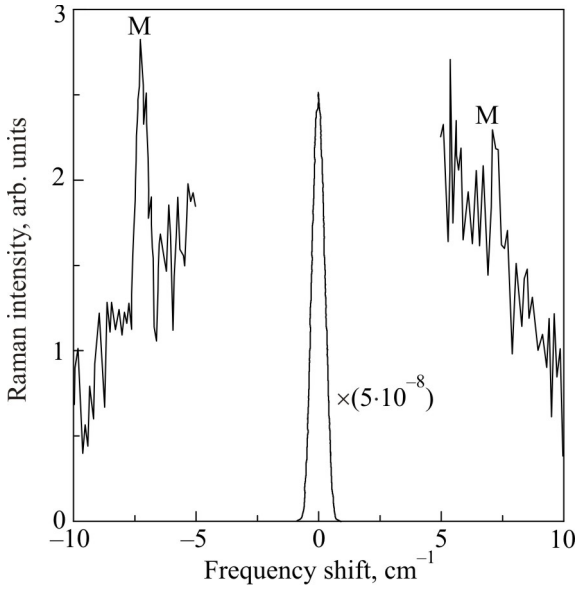

Fig. 3. One-magnon (M) Raman spectrum of MnF_2 at 41 K recorded in $X(ZX)Y$ polarization at a spectral resolution of 0.53 cm^{-1}.

values are for K_+ and G_+, whereas $I_S(ZX)$ will be different (unless $G_+/K_+ = 0$). It is seen that the intensity data points (allowing for an experimental uncertainty of 10 to 20% typically) broadly confirm this prediction and allow us to make a rough estimate for the ratio G_+/K_+. First, we note that in the absence of any quadratic coupling ($G_+/K_+ = 0$), the intensities for all three polarizations would be described by the broken curve in Fig. 4, which provides an inadequate fit to the data. A much better fit is provided if G_+/K_+ is small and positive, as illustrated by the solid lines for $G_+/K_+ = 0.08$ in Fig. 4, where the upper line refers to (XZ) and (YZ) polarizations and the lower line to (ZX) polarization.

Similarly, for the anti-Stokes data, the role of quadratic coupling is to enhance the intensities in certain polarizations (making it easier to study experimentally) and to modify the temperature dependence. In Fig. 5 it can be seen that the variation of $I_{AS}(ZX)$ is much better described by the solid theory curve for $G_+/K_+ = 0.08$ than by the broken curve for $G_+/K_+ = 0$. Further evidence that $G_+/K_+ \neq 0$ is provided by the intensity ratio I_{AS}/I_S in (ZX) polarization, where we have measurements at three different temperatures. Overall, from the temperature dependences of I_S and I_{AS} and from the behavior of I_{AS}/I_S, we deduce that G_+/K_+ lies approximately in the range 0.05 to 0.1.

The out-of-phase terms may also contribute to the scattered intensity [14] and we illustrate their effect by some numerical examples in Fig. 6, taking the case of linear magneto-optic coupling ($G_+ = G_- = 0$) and (XZ) polarization. Curves for in-phase scattering only ($K_- = 0$) and out-of-phase scattering only ($K_+ = 0$) are shown, together with an intermediate case. In fact, the predicted intensity I_S is sensitive to even a relatively small amount of out-of-phase scattering, because the coefficient of K_- in Eq. (11) is much larger than the coefficient of K_+ in Eq. (10) (since $\omega_E >> \omega_A$ for MnF_2). The admixture of in-phase and out-of-phase scattering corresponding to the case $|K_-/K_+| = 0.007$ in Fig. 6 is seen to give a good overall fit to the data across the temperature range.

The results indicate that while the linear magneto-optical coupling coefficient K_+ for in-phase scattering is dominant there is an important contribution due to the qua-

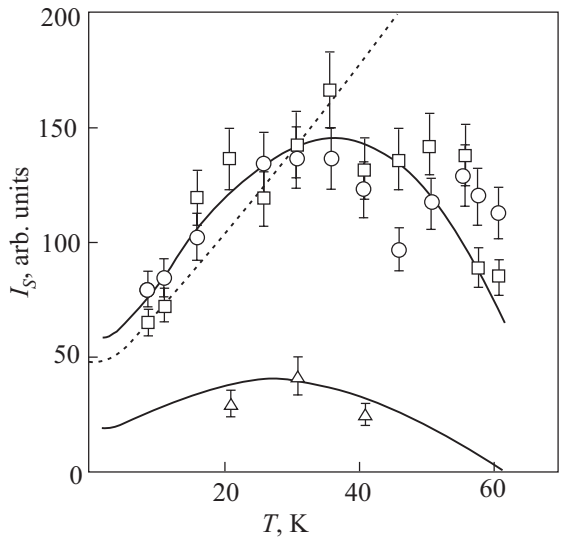

Fig. 4. Experiment and theory for the temperature dependence of the one-magnon integrated intensity in MnF_2 for Stokes scattering in several polarizations. The experimental points refer to, (XZ) polarization (○); (YZ) polarization (□); (ZX) polarization (Δ). The theory curves are for $G_+/K_+ = 0$ (broken line) and $G_+/K_+ = 0.08$ (solid lines).

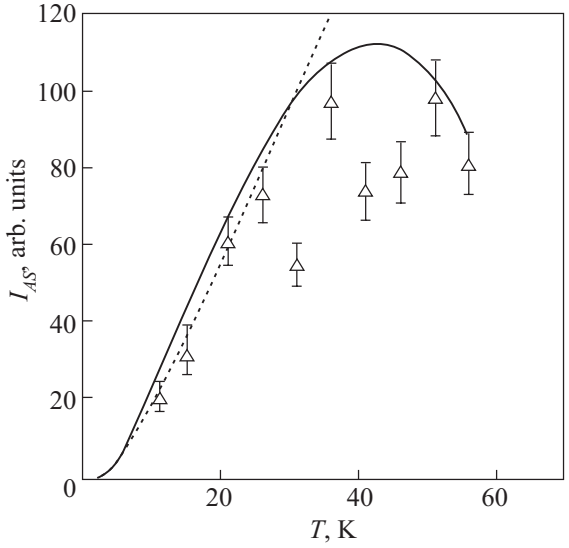

Fig. 5. Experiment and theory for the temperature dependence of the one-magnon integrated intensity in MnF_2 for anti-Stokes scattering. The experimental points (Δ) refer to (ZX) polarization. The theory curves are for $G_+/K_+ = 0$ (broken line) and $G_+/K_+ = 0.08$ (solid line).

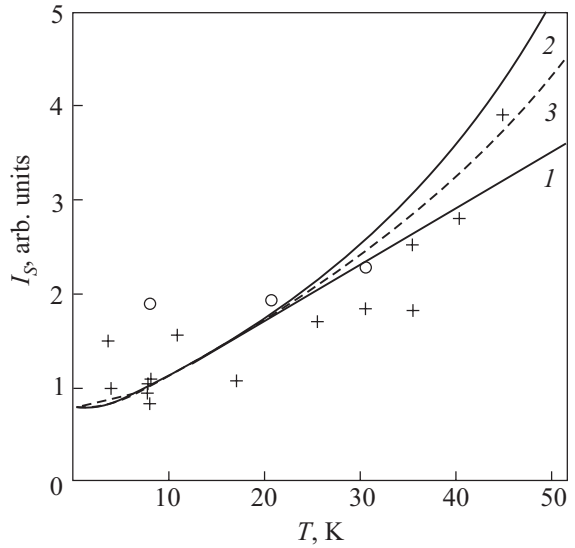

Fig. 6. Comparison of theory and experiment for the temperature dependence of the relative one-magnon integrated intensity (including the Bose population factor) in MnF_2. The theory curves are calculated taking the quadratic magnetooptic coefficients to be zero. The plotted curves correspond to: $K_- = 0$ (*1*); $K_+ = 0$ (*2*); $|K_-/K_+| = 0.007$ (*3*). The experimental data are from $Z(XZ)Y$ (crosses) and $Z(YZ)Y$ (circles) polarizations.

dratic in-phase coefficient G_+ and a very slight contribution from the out-of-phase linear magnetooptical coupling coefficient K_-. The G_+/K_+ and $|K_-/K_+|$ values obtained for MnF_2 are presented in Table 3 for easy comparison with the results obtained for the other antiferromagnets.

3.1.2. Two-magnon scattering. By comparison between theory and experiment for the two-magnon Stokes intensities at low temperatures (< 10 K) in various polarizations [14], we have been able to deduce the relative magnitudes of the magnetooptic coupling coefficients B_n ($n = 1, ..., 5$) appearing in Eq. (15). The results for MnF_2 are summarized in Table 4, where the values are quoted relative to the largest coefficient B_3. We were not able to deduce coefficients B_6 and B_7 for MnF_2 from the results of those measurements [16].

The two-magnon scattering in MnF_2 is considerably stronger than the one-magnon scattering. For example, the ratio of the integrated intensities of the two-magnon scattering in $Z(YX)Y$ polarization to the one-magnon scattering in $Z(XZ)Y$ polarization is 310 ± 25 at 8 K. From this ratio we can estimate the relative magnitudes of the linear and quadratic coupling coefficients K_+ and B_3, respectively. Using Eq. (4) for the one-magnon intensity and $T = 0$ expressions from Brya and Richards [18] for the two-magnon intensity, we deduce $K_+/B_3 \approx 0.5$ for excitation at 476.5 nm.

3.2. FeF_2

3.2.1. One-magnon scattering. The analysis of the one-magnon Raman scattering in FeF_2 is more complicated than was the case for MnF_2 owing to the pronounced asymmetric line shape of the conventional (acoustic) magnon peak and the presence of optic magnon peaks at higher temperatures [12]. From an extensive theoretical analysis the absolute value of G_+/K_+ was obtained from one-magnon Stokes and anti-Stokes scattering observed in $X(YZ)Y$ and $X(ZX)Y$ polarizations as a function of temperature for a number of different excitation wavelengths, as shown in Table 3. These results indicate a weak but significant dependence of G_+/K_+ on the wavelength; G_+/K_+ increases with increasing wavelength for light in the visible region. The origin of the effect is unclear, but it does not appear to correlate with the wavelength-dependence of the optical absorption [12] of FeF_2.

3.2.2. Two-magnon scattering. In Fig. 7 we compare theoretical and experimental spectra in $X(YX)Y$ polarization at low temperature [16]. Scattering in (YX) polarization is governed by magnetooptic coefficient B_3 and dotted line shows the theoretical fit (using the parameters in Table 2) to the two-magnon Raman spectrum and including just this term. However, to improve further the fit between theory and experiment for the (YX) polarization we need to consider the consequences of the sample X and Y axis orientation which are rotated about the c axis through an angle $\theta = 27^\circ$. If the interaction Hamiltonian H_{int} takes the form given in Eqs. (14) and (15) it is easily verified that the effect of the rotation only introduces an overall factor of

Table 3. Absolute and relative linear (K) and quadratic (G) magnetooptic coupling coefficients for one-magnon Raman scattering in rutile-structure antiferromagnets. The subscripts (+) and (–) refer to in-phase and out-of-phase scattering, respectively

Compound	Excitation wavelength, nm	$\lvert G_+\rvert$	$\lvert G_-\rvert$	$\lvert K_+\rvert$	$\lvert K_-\rvert$	$\lvert G_+/K_+\rvert$	$\lvert G_-/K_+\rvert$	$\lvert K_-/K_+\rvert$
FeF_2 (Ref. 12)	647.1	–	–	–	–	0.58	–	–
	514.5	–	–	–	–	0.49	–	–
	488.0	–	–	–	–	0.46	–	–
	476.5	–	–	–	–	0.44	–	–
	457.9	–	–	–	–	0.40	–	–
MnF_2 (Refs. 14 and 17)	476.5	–	~0	–	–	0.05–0.1	–	0.007
NiF_2 (Ref. 11)	514.5	~0	–	–	0	~1	0.25	–

Table 4. Relative magnetooptic coupling coefficients, B_n (n = 1, …, 7), for two-magnon Raman scattering in rutile-structure antiferromagnets.

Compound	Excitation wavelength, nm	$\|B_1/B_3\|$	$\|B_2/B_3\|$	$\|B_4/B_3\|$	$\|B_5/B_3\|$	$\|(B_4 \pm B_5)/B_3\|$	$\|B_6/B_3\|$	$\|B_7/B_3\|$	$\|B_6/B_7\|$
FeF_2 (Ref. 16)	514.5	–	0.3	0.8	~0	0.8	0.05	~0	–
MnF_2 (Ref. 17)	476.5	0.14	0.32	0.66	0.007	0.65–0.67	–	–	–
CoF_2 (Ref. 9)	800.0	0.2	0.6	–	–	0.7	–	–	0.3
NiF_2 (Ref. 9)	514.5	~0	0.2	–	–	0.5	–	–	–

$(\cos 2\theta)^2$ in the (YX) polarization intensity without affecting the line shape. However, there is an additional contribution to H_{int}, which is allowed by symmetry but generally neglected, governed by coupling coefficients B_6 and B_7 (see Sec. 2). When this additional term is rewritten in the laboratory X,Y,Z coordinate system we conclude that it allows a mixing in of various scattering contributions. Fleury and Loudon (Ref. 3) have shown that the yx and xy Raman tensor elements are equal for two-magnon scattering; thus B_7 must be negligibly small. The effect of the remaining B_6 term is to produce scattering of Γ_1^+ symmetry proportional to $(B_6 \sin 2\theta)^2$ and a cross term proportional to $B_3B_6 \sin 4\theta$. We have calculated this cross term and find that it peaks at about the same frequency as the Γ_4^+ mode but has a larger tail to low frequency. The theoretical spectrum with such a cross term included is shown in Fig. 7 by the broken curve, taking $B_6/B_3 = 0.05$. Even though the admixture of this cross term is small, it has led to an improved fit especially in the tails of the peak.

Likewise from the experimental spectra in (ZZ), (YX) and (ZX) polarizations at 12 K we have estimated the relative magnitudes of the optical coupling coefficients B_2, B_3, and B_4 in Eq. (15). We find $|B_4/B_3| = 0.8$ and $|B_2/B_3| = 0.3$.

Comparisons can also be made with the ratio of coefficients K_+/B_3 for FeF_2. From measurements of the one- and two-magnon scattering in FeF_2 using excitation wavelengths of 514.5 and 647.1 nm [12,16], we estimate

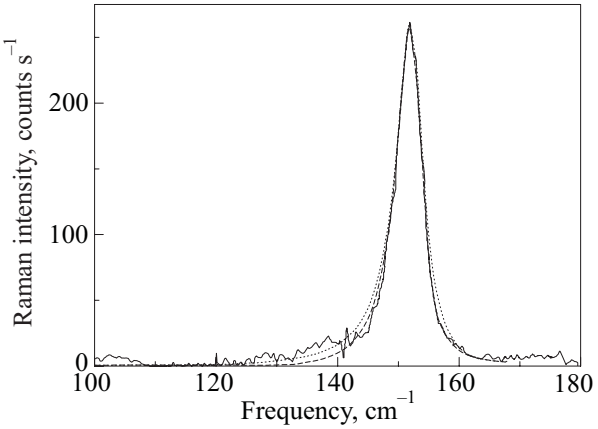

Fig. 7. The two-magnon part of the experimental $X(YX)Y$ spectrum for FeF_2 at 12 K (full curve) compared with the theoretical line shapes without (dotted curve) and with (broken curve) an additional cross term involving B_6.

$K_+/B_3 \approx 0.5$ in both cases. These estimates were obtained in the same manner as for MnF_2, but in addition allowing for the significant effect of the G_+ coefficient on the FeF_2 one-magnon intensity. The remarkable result is that the K_+/B_3 ratios are of the same order in MnF_2 and FeF_2.

3.3. CoF_2

3.3.1. One-magnon scattering. No results have been obtained to date on the one-magnon magnetooptic coefficients of CoF_2[10].

3.3.2. Two-magnon scattering. In Fig. 8,*a* we compare theory and experiment for the low-temperature ($T \sim 5$ K) two-magnon Raman intensities in $Y(XX)Z$ polarization [9]. By comparing theory with experiment for the integrated intensities in $Y(XX)Z$ polarization we are able to estimate the relative magnitudes of the magnetooptical coefficients B_1 and B_3. The theory curve is obtained using $|B_1/B_3| = 0.2$, which represents an upper limit for the magnitude of B_1 relative to B_3. The small contribution of the Γ_1^+ mode does not shift the peak frequency and its main effect is to increase the height of the tail of the peak at lower frequencies. The mixing of the Γ_1^+ and Γ_4^+ modes also leads to cross terms proportional to $B_1B_3 \sin 2\theta$. However, these terms cancel out on numerical integration over the Brillouin zone.

In Fig. 8,*b* we compare theory with experiment for the off-diagonal polarizations $X(ZX)Z$, $Y(ZX)Z$, and $Y(ZY)Z$, all of which represent the Γ_5^+ mode only. The rotation to the laboratory coordinate system does not produce any mixing effects because the crystal c axis coincides with the laboratory Z axis. The main effect of the rotation of the laboratory axes with respect to the crystal axes by 45° is to produce symmetric and antisymmetric combinations of the B_4 and B_5 magnetooptic coupling coefficients. The two-magnon scattering intensity is proportional to $|B_4 + B_5|^2$ for the (XZ) and (YZ) polarizations and to $|B_4 - B_5|^2$ for the (ZX) and (ZY) polarizations. These terms represent overall multiplicative factors that do not affect the line shapes of the spectra. The experimental spectra are effectively identical in all of these polarizations and thus we are unable to deduce the relative values of B_4 and B_5 for CoF_2 except to conclude that one of these must be far greater in magnitude than the other. By comparing the integrated intensities in Fig. 8,*a* and Fig. 8,*b* we are able to deduce that $|(B_4 \pm B_5)/B_3| \approx 0.7$. Also, making use of the data in $X(ZZ)Y$ polarization, we are able to deduce that $|B_2/B_3| \approx 0.6$.

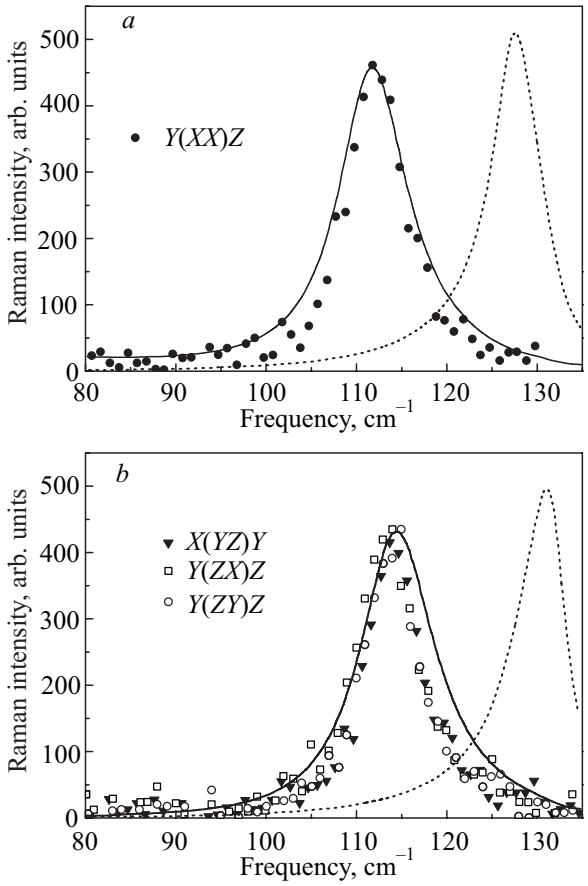

Fig. 8. Comparison of theory curve and experimental points for the low-temperature (~5 K) two-magnon Raman spectrum of CoF_2 in diagonal (*a*) and off-diagonal (*b*) polarizations, as indicated. The dotted lines show the theoretical results without the inclusion of magnon–magnon interactions.

The experimental spectrum in $X(YX)Y$ polarization reveals a two-magnon peak frequency at (113 ± 1) cm^{-1} and an integrated intensity that is ~10% of the integrated intensity in other off-diagonal polarizations. The terms involving the (*YX*) polarization in Eq. (16) vanish for a rotation through an angle of 45°, and thus the intensity for this polarization [as well as the (*XY*) polarization] is expected to be much weaker than in other off-diagonal polarizations. The origin of the two-magnon feature in the (*YX*) polarization may be attributed to a small misalignment of the axes and/or to the additional interaction term in Eq. (16), which involves different combinations of the incident and scattered polarizations. When $\varphi'(\boldsymbol{\delta})$ is rewritten with respect to the laboratory coordinate system the scattering intensity will depend on the additional magnetooptical coefficients B_6 and B_7. By comparing theory with experiment we are able to estimate the relative values of the magnetooptical coefficients and we find $|B_6/B_7| \approx 0.3$.

3.4. NiF_2

3.4.1. One-magnon scattering. In Fig. 9 we compare theory and experiment for the one-magnon scattering from the upper branch in (*YZ*) polarization for different values of the ratio $|G_+/K_+|$ [11]. Here we show results for in-phase scattering, i.e., with $K_- = G_- = 0$ as for equivalent sublattices. It is noteworthy that theory curve *1*, for which $G_+ = 0$, does not decrease even as the temperature increases to 0.9 T_N. This can be understood from Eq. (38) of Ref. 11, because the decrease in the sublattice spin average is compensated by the increase in the thermal population factor. In the case of out-of-phase scattering the calculated line shapes are not very sensitive to the ratio $|G_-/K_-|$.The experimental data in Fig. 9 show that the integrated intensity has a relatively weak dependence on temperature throughout the experimental range, which is indicative of a value for $|G_+/K_+|$ of the order of 1. The theory curves for the Stokes intensity of the upper branch in NiF_2 are qualitatively similar to those obtained in Ref. 14 for the one-magnon scattering in MnF_2. In Fig. 10 we show results in (*YZ*) polarization for the temperature dependence of the anti-Stokes to Stokes intensity ratio for the lower energy branch. The theoretical results here are in qualitative agreement with experimental data if we include effects of the magneto-optical coefficient G_-. The theory curves are obtained taking $G_+ = K_- = 0$ and indicate that $|G_-/K_+| = 0.25$.

We now consider the off-diagonal (*YX*) polarization. For this polarization two new magnetooptic coupling coefficients need to be introduced; K_3 and G_3 [11]. Setting $G_3 = 0$ results in the contribution to the integrated intensity due to the upper branch vanishing. When the quadratic

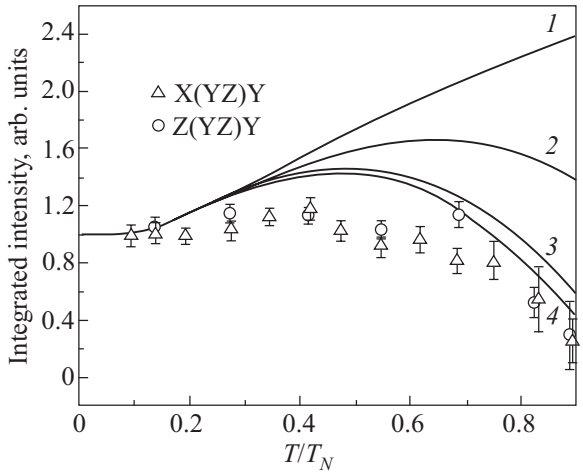

Fig. 9. Comparison of theory and experiment for the temperature dependence of the Stokes integrated intensity in NiF_2 for the upper branch in (*YZ*) polarization. The theory curves are obtained for the following values of $|G_+/K_+|$: 0.0 (*1*), 0.1 (*2*), 1 (*3*), and 100 (*4*).

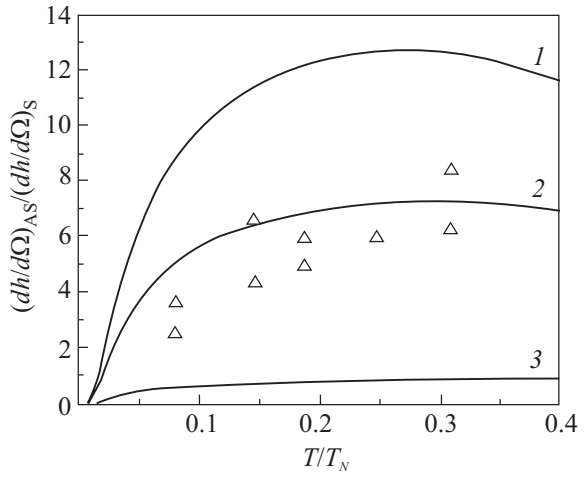

Fig. 10. Comparison of the NiF_2 lower energy branch anti-Stokes to Stokes integrated intensity ratio in (*YZ*) polarization for different values of $|G_-/K_+|$: 0.30 (*1*), 0.25 (*2*), and 0 (*3*).

magnetooptic coefficient G_3 is included, it is found that the intensity contribution due to the upper branch is quadratic in the spin canting angle and thus may be neglected because of the small canting angle in NiF_2. This theoretical prediction is consistent with the fact that the upper branch one-magnon scattering was not observed experimentally in the Raman spectra recorded in (*YX*) polarization [11].

In Fig. 11 we plot the calculated anti-Stokes to Stokes integrated intensity ratio in (*YX*) polarization for the lower branch and we compare theoretical results with the experimental data. We show theory curves for different values of the relative magnetooptic coupling coefficients $|G_3/K_3|$. We find qualitative agreement between theory and experiment when $|G_3|$ is small compared to $|K_3|$, as expected. Qualitatively similar results are obtained in the case of (*XY*) polarization.

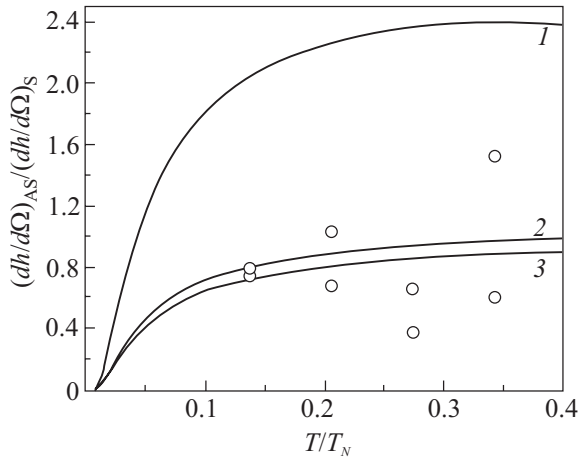

Fig. 11. Comparison of theory with experiment for the temperature dependence of the lower energy branch anti-Stokes to Stokes integrated intensity ratio in NiF_2 for (*YX*) polarization. The theory curves correspond to $|G_3/K_3|$ values of: 1.0 (*1*), 0.1 (*2*), and 0 (*3*).

3.4.2. Two-magnon scattering. In Fig. 12,*a* we compare theory with experiment for the *Z*(*XX*)*Y* diagonal polarization [9]. The solid line represents the Γ_4^+ mode only and is obtained using our optimal set of parameters for NiF_2 given in Table 2. The dotted line represents the theory curve without the inclusion of magnon–magnon interactions. The theoretical two-magnon peak frequencies for the Γ_4^+ and Γ_5^+ modes are 203.3 cm^{-1} and 203.7 cm^{-1}, respectively. For comparison, the dashed line shows the predicted two-magnon intensity using the set of parameters of Ref. 19. Here the height of the spectrum is scaled to coincide with the experimental maximum intensity. Although the theory predicts some mixing of the Γ_1^+ and Γ_4^+ modes in this polarization we obtain a very good fit to the experimental data without any admixture of the Γ_1^+ mode, implying that the magnitude of the magnetooptical coefficient $|B_1| << |B_3|$.

In Fig. 12,*b* we compare theory with experiment for the off-diagonal polarizations *X*(*YZ*)*Y*, *X*(*ZX*)*Y*, and *Z*(*YZ*)*Y*. All of these experimental polarizations investigate the Γ_5^+ mode only. As in CoF_2, the experimental spectra in these polarizations have similar line shapes and integrated inten-

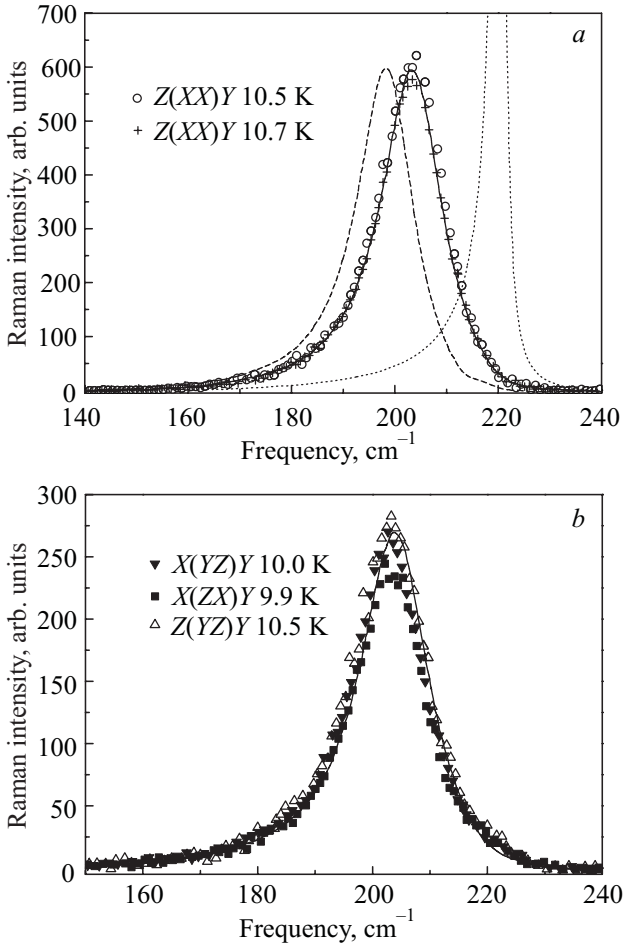

Fig. 12. Comparison of theory curves (see text) and experimental points for the low-temperature (~10 K) two-magnon Raman spectrum of NiF_2 in diagonal (*a*) and off-diagonal polarizations (*b*), as indicated.

sities and thus we are unable to deduce relative values of the magneto-optical coefficients B_4 and B_5 except to conclude that one is far greater in magnitude than the other. By comparing the integrated intensities in the different off-diagonal polarizations we find that $|(B_4 \pm B_5)/B_3| \approx 0.5$.

The weaker scattering observed in $X(YX)Y$ polarization may be attributed to the 45° rotation of the experimental axes with respect to the crystal axes. Allowing for the possibility of a small misalignment of the axes we expect a weak scattering signal with the spectral features of the Γ_4^+ mode. The similarly weak scattering spectrum observed in the diagonal polarization $X(ZZ)Y$ gives an asymmetric line shape with a peak frequency that is ~10 cm^{-1} greater than the peak frequencies observed in other polarizations. A similar feature was observed for the two-magnon spectrum in the (ZZ) polarization in FeF_2 [16]. The calculated spectrum for the (ZZ) polarization appears as a flat non-resonant band because of weighting of the zone-center point and does not account well for the peak feature observed in the experimental measurement. Nevertheless, from the integrated intensity we deduce that $|B_2/B_3| \approx 0.2$.

4. Discussion of magnetooptic coupling parameters

4.1. One-magnon coefficients

From a theoretical analysis of the integrated intensity as a function of temperature of the very weak one-magnon scattering in MnF_2 we have shown that in-phase linear magnetooptic coupling (involving the coefficient K_+) provides the dominant effect, although small admixtures due to quadratic magnetooptic coupling and out-of-phase scattering may also be present (see Table 3). This contrasts with the one-magnon scattering from another rutile-structure antiferromagnet, FeF_2, which has also been studied in detail. In FeF_2 the one-magnon scattering is much stronger and in-phase quadratic magnetooptic coupling plays an important role. The relative weakness of the one-magnon scattering in MnF_2 can be partly attributed to the small value of ω_A, which weights K_+ in Eq. (10), and partly due to differences in the magnetooptic coefficients for MnF_2 and FeF_2. For example, from Raman data on MnF_2 (Ref. 14) and FeF_2 (Ref. 12) recorded under similar conditions, we find for the ratio of one-magnon integrated intensities at approximately 10 K that

$$I_S(MnF_2)/I_S(FeF_2) \sim 10^{-2}. \quad (18)$$

On the basis of linear magnetooptic coupling only it can then be estimated that $K_+(MnF_2)/K_+(FeF_2) = 0.2$. However, if the quadratic magnetooptic coupling in FeF_2 is properly taken into account [using Eqs. (9), (10), and (11)], we find that $K_+(MnF_2)$ and $K_+(FeF_2)$ become more comparable in magnitude. We conclude that the quadratic coupling term has the effect of enhancing the intensity in FeF_2 relative to MnF_2. Because of the weak magnetooptic coupling and the low frequency of the magnon in MnF_2, it would be extremely difficult to observe any critical effect in the one-magnon scattering near T_N using the Raman technique. However, such critical scattering may be observable with the Brillouin technique, as applied for example to $KNiF_3$ [20].

As can be seen from Table 3, the in-phase and out-of-phase quadratic magnetooptic coefficients for NiF_2 play an even more significant role in determining the strength of the one-magnon scattering intensity compared with MnF_2 and FeF_2. This may, in part, be attributable to the canting and its weak associated ferromagnetic moment in NiF_2, which do not occur in the other materials.

However, the out-of-phase linear and quadratic magnetooptic coefficients are generally negligible for antiferromagnets with the rutile structure and in-phase linear coupling is the major contribution to the scattering intensity.

Interestingly, in the one wavelength dependent study performed so far, $|G_+/K_+|$ for FeF_2 was found to increase with increasing wavelength (see Table 3). The origins of this behavior could be found from comparisons with results from further measurements of the magnetic birefringence and field-dependent Faraday rotation in FeF_2. Similar studies would be worth carrying out for the other antiferromagnets. Additional details of the coupling mechanisms could also be obtained from inelastic light scattering studies of these transition-metal fluorides in an external magnetic field.

4.2. Two-magnon coefficients

As can be seen from Table 4, the relative B coefficients for MnF_2 are quite similar to those of FeF_2, and the same is true for the absolute scattering intensities. The ratio of the integrated intensities of the Γ_5^+ two-magnon scattering in MnF_2 (476.5 nm excitation) and FeF_2 (514.5 nm excitation) is 0.82 ± 0.05. The corresponding ratio is 0.52 ± 0.03 with excitation at 647.1 nm for FeF_2. In deriving these ratios, corrections have been made for the frequency-to-the-fourth-power scattering law, but the spectrometer and photomultiplier responses have not been included. As the combined spectrometer and detector response is almost flat around 500 nm and then slowly falls with increasing wavelength, it is not possible to attribute the difference between the above ratios to mainly instrumental effects. There must also be a major contribution from the wavelength dependence of the scattering in FeF_2, which has already been noted for the one-magnon scattering. Another point of note is that the coefficient ratio K_+/B_3 is about the same for both MnF_2 and FeF_2.

The magnetooptic coupling coefficients obtained for CoF_2 and NiF_2 are broadly similar to those found for MnF_2 and FeF_2 (see Table 4).

5. Conclusion

In conclusion, this first detailed comparison of the magnitudes of the various coupling coefficients for four rutile-structure compounds has revealed surprising similarities in many coefficients. In one-magnon Raman scattering, the in-phase linear magnetooptic coefficient dominates and the main differences between MnF_2, FeF_2, and NiF_2 lie in the relative significance of the in-phase quadratic magnetooptic coefficient. Thus the quadratic coefficients are now seen to be of particular importance in determining the strength of the one-magnon scattering in a variety of insulators. The role of quadratic magnetooptic coupling has been demonstrated also for other iron compounds, in particular, including $Y_3Fe_5O_{12}$, $FeCl_2$, and $FeBr_2$. It would be informative to make similar detailed comparisons with antiferromagnets possessing these and other crystal structures, but containing a variety other metal ions, to quantify further the relative significance of the linear and quadratic terms.

In two-magnon Raman scattering, magnetooptic coefficient B_3 dominates for all of these antiferromagnets. However, each of the other coefficients are remarkably similar in magnitude, in general, and not negligible in most cases, indicating some universality in the way light interacts with the pairs of magnons of opposite and equal wave vector created in antiferromagnets having the rutile-structure crystal symmetry.

We thank our many collaborators, who are listed in the references given below, for their valuable contributions to the work reported here.

1. C.V. Raman and R.S. Krishnan, *Nature* **121**, 501 (1928).
2. M.G. Cottam and D.J. Lockwood, *Light Scattering in Magnetic Solids,* Wiley, New York (1985).
3. P.A. Fleury and R. Loudon, *Phys. Rev*. **166**, 514 (1968).
4. M.G. Cottam, *J. Phys.* **C8**, 1933 (1975).
5. W. Wettling, M.G. Cottam, and J.R. Sandercock, *J. Phys.* **C8**, 211 (1975).
6. G. Mischler, D. Bertrand, D.J. Lockwood, M.G. Cottam, and S. Legrand, *J. Phys.* **C14**, 945 (1981).
7. G.C. Psaltakis and M.G. Cottam, *J. Phys*. **C15**, 4847 (1982).
8. G.C. Psaltakis, G. Mischler, D.J. Lockwood, M.G. Cottam, A. Zwick, and S. Legrand, *J. Phys.* **C17**, 1735 (1984).
9. E. Meloche, M.G. Cottam, and D.J. Lockwood, *Phys. Rev*. **B76**, 104406 (2007).
10. E. Meloche, M.G. Cottam, and D.J. Lockwood, *to be published*.
11. E. Meloche, M.G. Cottam, V.P. Gnezdilov, and D.J. Lockwood, *Phys. Rev*. **B81**, 024426 (2010).
12. D.J. Lockwood, M.G. Cottam, V.C.Y. So, and R.S. Katiyar, *J. Phys.* **C17**, 6009 (1984).
13. A.L. Awang and M.G. Cottam, *J. Phys*. **C12**, 121 (1979).
14. D.J. Lockwood and M.G. Cottam, *Phys. Rev*. **B35**, 1973 (1987).
15. J. Ariai, P.A. Bates, M.G. Cottam, and S.R.P. Smith, *J. Phys.* **C15**, 2767 (1982).
16. M.G. Cottam, V.C.Y. So, D.J. Lockwood, R.S. Katiyar, and H.J. Guggenheim, *J. Phys.* **C16**, 1741 (1983).
17. M.G. Cottam, V.P. Gnezdilov, H.J. Labbé, and D.J. Lockwood, *J. Appl. Phys*. **76**, 6883 (1994).
18. W.J. Brya and P.M. Richards, *Phys. Rev*. **B9**, 2244 (1974).
19. M.T. Hutchings, M.F. Thorpe, R.J. Birgeneau, P.A. Fleury, and H.J. Guggenheim, *Phys. Rev*. **B2**, 1362 (1970).
20. K.B. Lyons and P.A. Fleury, *Phys. Rev. Lett*. **48**, 202 (1982).